materials

MDPI

Article

Mechanism for Improved Curie Temperature and Magnetic Entropy Change in Sm-Doped $Fe_{88}Zr_8B_4$ Amorphous Alloys

Zhe-Rui Zhang [1], Xiang-Jie Liu [1], He-Teng Zhang [1], Qiang Wang [1], Ding Ding [1], Ben-Zhen Tang [2], Peng Yu [2], Jin-Lei Yao [3] and Lei Xia [1,*]

[1] Institute of Materials & Laboratory for Microstructure, Shanghai University, Shanghai 200072, China; zhangzherui@shu.edu.cn (Z.-R.Z.); liuxiangjie@shu.edu.cn (X.-J.L.); 22722611@shu.edu.cn (H.-T.Z.); mat_wq@shu.edu.cn (Q.W.); d.ding@shu.edu.cn (D.D.)

[2] Chongqing Key Laboratory of Photo-Electric Functional Materials, College of Physics and Electronic Engineering, Chongqing Normal University, Chongqing 401331, China; bz.tang@cqnu.edu.cn (B.-Z.T.); pengyu@cqnu.edu.cn (P.Y.)

[3] Jiangsu Key Laboratory of Micro and Nano Heat Fluid Flow Technology and Energy Application, School of Physical Science and Technology, Suzhou University of Science and Technology, Suzhou 215009, China; jlyao@usts.edu.cn

* Correspondence: xialei@shu.edu.cn; Tel.: +86-021-6613-5067

Abstract: In the present work, $Fe_{88}Zr_{8-x}Sm_xB_4$ (x = 2, 4) amorphous alloys (AAs) were successfully synthesized into the shape of 40-micrometer-thick ribbons and their magnetic properties were measured. The $Fe_{88}Zr_{8-x}Sm_xB_4$ (x = 2, 4) AAs exhibited a rather high maximum magnetic entropy change ($-\Delta S_m^{peak}$): ~3.53 J/(K × kg) near 317 K for x = 2 and ~3.79 J/(K × kg) near 348 K for x = 4 under 5 T. The effects of a Sm substitution for Zr on the Curie temperature (T_c) and $-\Delta S_m^{peak}$ were studied and compared to those of Nd and Pr substitutions, for the purpose of revealing the mechanism involved in more detail.

Keywords: amorphous alloy; glass formation ability; Curie temperature; magnetocaloric effect; magnetic entropy change

Citation: Zhang, Z.-R.; Liu, X.-J.; Zhang, H.-T.; Wang, Q.; Ding, D.; Tang, B.-Z.; Yu, P.; Yao, J.-L.; Xia, L. Mechanism for Improved Curie Temperature and Magnetic Entropy Change in Sm-Doped $Fe_{88}Zr_8B_4$ Amorphous Alloys. *Materials* **2023**, *16*, 7274. https://doi.org/10.3390/ma16237274

Academic Editor: Jana Bidulská

Received: 21 October 2023
Revised: 8 November 2023
Accepted: 14 November 2023
Published: 22 November 2023

1. Introduction

With global warming and the increasing population, the demand for air conditioners has increased dramatically in recent years. Conventional vapor compression/expansion refrigeration technology, which is currently the major technology for room-temperature refrigeration, has several disadvantages, such as a low efficiency and environmental unfriendliness. For example, the energy utilization efficiency of traditional refrigeration technology is generally less than 10%, and its refrigerant (freon) is harmful to the ozone layer and leads to holes in the ozone layer, which, in turn, exacerbates global warming [1–4]. Therefore, it is vitally urgent to improve refrigeration with a novel solution that is not harmful to the environment and has a higher efficiency.

Magnetic refrigeration (MR) technology, using magnetocaloric materials as solid refrigerants, avoids most of the disadvantages of traditional refrigeration technology. For instance, the efficiency of MR technology is much higher and refrigerators that use MR technology are more compact due to the solid refrigerant [3–7]. In addition, MR technology is friendly to the environment because it is free of ozone-depleting gas [6,7]. The application perspective of MR technology depends mainly on the magnetocaloric property of the magnetic refrigerant. The magnetocaloric property, namely the magnetocaloric effect (MCE), is an intrinsic property of magnetic materials that was first observed in iron by E. Warburg in 1881 [8]. The magnetic entropy of a magnet decreases with the ordering of magnetic moments upon magnetization, and increases with demagnetization. The decrease/increase in magnetic entropy under adiabatic conditions leads to the heating/cooling of the magnet, which can be applied to achieve refrigeration.

Magnetocaloric materials can generally be sorted into two categories according to the magnetic phase transition (MPT) that they experience near their Curie temperature (T_c), or the shape of their magnetic entropy change ($-\Delta S_m$) curves. Materials undergoing a first-order MPT show a sharp $-\Delta S_m$ curve, which results in an ultra-high maximum $-\Delta S_m$ ($-\Delta S_m{}^{peak}$), but a narrow working temperature range and a low refrigeration capacity (*RC*) [9–13]. In contrast, second-order MPT materials show a broadened $-\Delta S_m$ curve that brings about a rather high *RC* and a wide working temperature range, both of which make second-order MPT materials more suitable to be used as refrigerants in magnetic refrigeration appliances, because a broadened $-\Delta S_m$ profile is vital for an Ericsson cycle [14–19]. As one of the important categories of second-order MPT materials, amorphous alloys (AAs) show unique characteristics that make them more suitable as magnetic refrigerants, such as formability within a wide compositional range and a tunable T_c as a result, better mechanical properties and corrosion resistance than their crystalline counterparts, low eddy current loss due to their high electric resistance, low hysteresis loss due to their excellent soft magnetic properties, and so on [20–22]. Amorphous magnetocaloric alloys are generally divided into two groups: rare-earth (RE)-based and transition-metal (TM)-based AAs. RE-based AAs, especially Gd-based AAs, show excellent glass formability (GFA) and outstanding magnetocaloric properties with a rather high $-\Delta S_m{}^{peak}$ at low temperatures [17,19,23,24]. However, the GFA and $-\Delta S_m{}^{peak}$ of these AAs decrease dramatically with their increasing T_c, and thus, Gd-based AAs with a T_c near room temperature exhibit a very low $-\Delta S_m{}^{peak}$ and a poor GFA, which makes them hard to fabricate [25–27]. In contrast, TM-based AAs, represented by Fe-based AAs, exhibit a fairly good GFA and can be easily prepared within a wide compositional range, which makes their T_c tailorable within the operating temperature interval of a domestic refrigeration appliance [28–35]. The shortcoming of Fe-based AAs is their low $-\Delta S_m{}^{peak}$; for example, the $-\Delta S_m{}^{peak}$ under 5 T of Fe-Zr-B ternary glassy alloys is usually not higher than 3.3 J/(K × kg) near room temperature [28,29]. As a consequence, one of the key issues for AAs applied industrially in MR is how to improve the $-\Delta S_m{}^{peak}$ to make it as high as possible near room temperature.

It is well known that microalloying is a useful way to achieve a better GFA and physical properties of AAs. In our preliminary works, we added a small amount of various elements and successfully improved the magnetocaloric performance of the Fe-Zr-B ternary AAs [31,32]. For instance, the $-\Delta S_m{}^{peak}$ under 5 T of $Fe_{88}Zr_8B_4$ AAs was enhanced to ~3.42 J/(K × kg) by a minor Co addition and was further improved to ~3.55 J/(K × kg) by a minor Nb addition [31]. A minor Sm substitution for the Fe of $Fe_{88}Zr_8B_4$ AAs led to an enhanced $-\Delta S_m{}^{peak}$ up to 3.55 J/(K × kg) [31]. However, microalloying by the substitution of other elements for Fe is finite for the improvement in the $-\Delta S_m{}^{peak}$.

More recently, we found that the $-\Delta S_m{}^{peak}$ of Fe-Zr-B ternary AAs was further increased by a minor substitution of RE elements for the Zr, and a larger $-\Delta S_m{}^{peak}$ was achieved in the $Fe_{87}Ce_8B_5$ AA ribbon (3.65 J/(K × kg) at 282.5 K) [33], $Fe_{88}Zr_4Pr_4B_4$ glassy ribbon (4.0 J/(K × kg) at 323 K) [34], and $Fe_{88}Zr_4Nd_4B_4$ glassy ribbon (4.1 J/(K × kg) at 335 K) [35]. The Sm element, with similar characteristics to Pr and Nd, also seemed to be a good substitute for Zr in improving the magnetocaloric performance of Fe-Zr-B AAs. Additionally, the mechanism for the effect of various kinds of RE substitutions on the magnetic and magnetocaloric performance has not been systematically investigated, and an understanding of the magnetocaloric performance of Fe-based AAs with various RE elements is helpful for developing better Fe-based magnetocaloric AAs with a high $-\Delta S_m{}^{peak}$ within the operating temperature interval of a domestic magnetic refrigerator. In the present work, we studied the effect of a Sm substitution for Zr on the GFA and the magnetic and magnetocaloric performance of $Fe_{88}Zr_8B_4$ AAs. Based on the experimental results obtained in this work and our previous works, the mechanism for the effect of an RE substitution on the T_c and $-\Delta S_m{}^{peak}$ of an $Fe_{88}Zr_8B_4$ basic alloy was investigated in more details.

2. Experimental Procedures

By arc-melting Fe, Zr, and Sm metal blocks (purity > 99.9 at.%) and an Fe-B pre-alloy at least four times, ingots with nominal compositions of $Fe_{88}Zr_{8-x}Sm_xB_4$ (x = 2, 4) were synthesized in a high-vacuum furnace protected by an Ar atmosphere. Due to the evaporation amount of the Sm element accounting for almost 4.39 wt.% of the total mass of the ingot during the arc-melting process, the actual concentration of Sm in the alloy ingots was estimated to be 1.91 at.% when x = 2 and 3.83 at.% when x = 4. Considering that there was not a significant deviation in the Sm concentration, the nominal composition of the two alloys is still used in the following text. The $Fe_{88}Zr_{8-x}Sm_xB_4$ (x = 2, 4) ribbons were prepared using a melt-spinning technology at a rotation rate of ~55 m/s. The distance from the nozzle to the wheel was about 2 mm and the melts were ejected onto the wheel surface under an ejection pressure of 0.5 MPa when the alloy melts were flowable. The $Fe_{88}Zr_{8-x}Sm_xB_4$ (x = 2, 4) as-quenched ribbons with an average thickness of approximately 40 μm were picked for subsequent investigations. The amorphous characteristics of the samples were firstly examined with a PANalytical X-ray diffractometer (XRD, Panalytical, Netherlands) using Cu K_α radiation, and further ascertained using the differential scanning calorimetry (DSC) curves measured using a NETZSCH 404 C calorimeter (Netzsch, Selb, Germany). The thermal properties of the AAs were obtained from the DSC curves measured at a heating rate of 0.333 K/s. A microstructural observation of the $Fe_{88}Zr_6Sm_2B_4$ amorphous ribbon was performed using a JEOL JEM-F200 cold field emission high-resolution electron microscope (HREM, JEOL, Tokyo, Japan). The HREM sample was polished using a GATAN 691 precision ion-polishing system (Ametek, Berwyn, PA, USA). A vibrating sample magnetometer (VSM) module on a Quantum Design model 6000 physical properties measurement system (PPMS, Quantum Design, San Diego, CA, USA) was employed for the magnetic measurements of the ribbons.

3. Results

3.1. The Structure of the $Fe_{88}Zr_{8-x}Sm_xB_4$ (x = 0, 2, 4) as-Quenched Ribbons

The XRD patterns of the $Fe_{88}Zr_{8-x}Sm_xB_4$ (x = 0, 2, 4) as-quenched ribbons are illustrated in Figure 1a. The smooth amorphous diffraction peak near 43 degrees and the invisible crystalline peaks suggested that these ribbons were amorphous. The sharp exothermic crystallization peak followed by the smooth endothermic glass transition hump in these DSC traces of ribbons, as shown in Figure 1b, also ascertained their amorphous characteristics.

3.2. Thermal Properties and GFA of the $Fe_{88}Zr_{8-x}Sm_xB_4$ (x = 0, 2, 4) AAs

The thermal properties of the $Fe_{88}Zr_{8-x}Sm_xB_4$ (x = 2, 4) AAs, including the onset temperature of the glass transition (T_g^{onset}) and primary crystallization (T_x^{onset}), were identified, as labeled on the three DSC traces of ribbons in Figure 1b. For comparison, the DSC trace of the $Fe_{88}Zr_8B_4$ basic alloy is also shown in Figure 1b. The addition of Sm obviously enlarged the supercooled liquid region ($\Delta T_x = T_x^{onset} - T_g^{onset}$) [36] of the $Fe_{88}Zr_8B_4$ amorphous alloy, which indicated an increased thermal stability against crystallization. The large ΔT_x of ~150 K for the $Fe_{88}Zr_{8-x}Sm_xB_4$ (x = 2, 4) AAs was much higher than those of the other Fe-Zr-B-based amorphous ribbons listed in Table 1, or even comparable to those of some Zr-based bulk metallic glasses [37]. The liquidus temperatures (T_l) of the $Fe_{88}Zr_{8-x}Sm_xB_4$ AA ribbons obtained from their melting curves, as displayed in the inset of Figure 1b, were approximately 1566 K for x = 2 and 1498 K for x = 4. Thus, the reduced glass transition temperature (T_{rg}, defined as the ratio of T_g^{onset} to T_l) [38] and the parameter γ ($=T_x^{onset}/(T_g^{onset} + T_l)$) [39] of the $Fe_{88}Zr_{8-x}Sm_xB_4$ AA ribbons were determined to be 0.453 and 0.378 for x = 2, and 0.478 and 0.390 for x = 4. Although the T_{rg} of the $Fe_{88}Zr_{8-x}Sm_xB_4$ (x = 2, 4) AAs was not as large as that of the $Fe_{88}Zr_8B_4$ alloy (T_{rg} = 0.489) [31], their γ was much larger than that of the $Fe_{88}Zr_8B_4$ alloy (γ = 0.350) due to the enlarged supercooled liquid region. Furthermore, the γ values of the $Fe_{88}Zr_{8-x}Sm_xB_4$ AAs were also much larger than that of other Fe-Zr-B-based AAs, as listed in Table 1, which made the $Fe_{88}Zr_{8-x}Sm_xB_4$ AAs exhibit a very large theoretical value of critical section

thickness (Z_c, ~1.96 mm for x = 2 and ~3.24 mm for x = 4) [39], even though the T_{rg} of the $Fe_{88}Zr_{8-x}Sm_xB_4$ AAs was not high enough. As a result, the large values of ΔT_x, γ, and Z_c of the $Fe_{88}Zr_{8-x}Sm_xB_4$ AAs indicated that they showed a better thermal stability than other Fe-Zr-B-based amorphous ribbons and a sufficient GFA for the preparation of continuous amorphous ribbons.

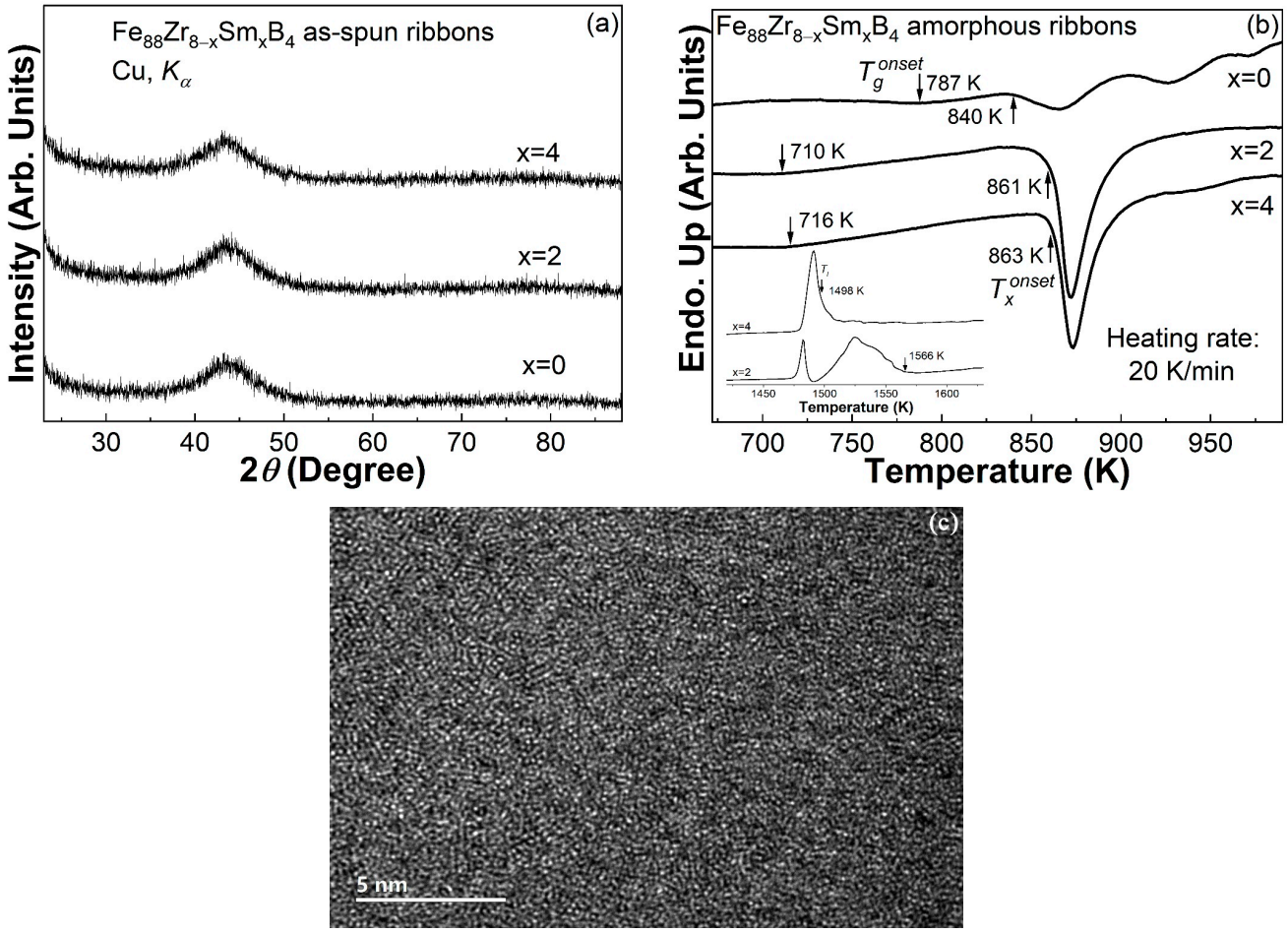

Figure 1. (**a**) The XRD patterns of the $Fe_{88}Zr_{8-x}Sm_xB_4$ (x = 0, 2, 4) as-spun ribbons; (**b**) the DSC curves of the $Fe_{88}Zr_{8-x}Sm_xB_4$ (x = 0, 2, 4) amorphous ribbons, with the melting behaviors in the inset; and (**c**) the HREM image of the $Fe_{88}Zr_6Sm_2B_4$ amorphous ribbon.

Table 1. The thermal parameters ΔT_x, T_{rg}, γ, and Z_c of some Fe-Zr-B-based amorphous alloys.

Composition	T_g^{onset} (K)	T_x^{onset} (K)	T_l (K)	ΔT_x (K)	T_{rg}	γ	Z_c (mm)	Refs.
$Fe_{88}Zr_6Sm_2B_4$	710	861	1566	151	0.453	0.378	1.96	Present work
$Fe_{88}Zr_4Sm_4B_4$	716	863	1498	147	0.478	0.390	3.24	
$Fe_{88}Zr_8B_4$	787	840	1611	53	0.489	0.35	0.61	
$Fe_{87}Co_1Zr_8B_4$	776	834	1580	58	0.491	0.354	0.72	
$Fe_{86}Co_2Zr_8B_4$	780	835	1574	55	0.496	0.355	0.75	
$Fe_{87}Zr_7B_4Co_2$	754	808	1570	54	0.48	0.348	0.56	[31]
$Fe_{85}Co_3Zr_5B_4Nb_3$	701	813	1495	112	0.469	0.370	1.41	
$Fe_{87}Zr_8B_4Sm_1$	828	859	1582	31	0.52	0.356	0.78	
$Fe_{86}Zr_8B_4Sm_2$	818	870	1580	52	0.52	0.363	1.05	
$Fe_{85}Zr_8B_4Sm_3$	828	883	1578	55	0.53	0.367	1.24	
$Fe_{88}Zr_6B_4Ti_2$	752	812	1539	60	0.489	0.354	0.72	[32]
$Fe_{88}Zr_6Pr_2B_4$	757	866	1509	109	0.482	0.377	1.88	[34]
$Fe_{88}Zr_4Pr_4B_4$	768	865	1527	97	0.503	0.372	1.53	

It has been reported that the presence of nanocrystals promotes heterogeneous nucleation during crystallization and weakens the thermal stability of AAs [40], while the XRD and DSC results may not distinguish a small number of small-sized nanoparticles [41]. Therefore, in order to further confirm the amorphous structure of the two ribbons, the $Fe_{88}Zr_6Sm_2B_4$ amorphous ribbon with a lower GFA was employed for HREM observation. There were no obvious nanoparticles or a long-range order, but only 1~2 nm of a short-range order in the disordered matrix, as shown in Figure 1c, implying a fully amorphous state of the $Fe_{88}Zr_6Sm_2B_4$ ribbon.

3.3. Magnetic Properties of the $Fe_{88}Zr_{8-x}Sm_xB_4$ (x = 0, 2, 4) AAs

The magnetization vs. temperature (*M-T*) curves of the $Fe_{88}Zr_{8-x}Sm_xB_4$ (x = 0, 2, 4) amorphous ribbons were measured from 200 K to 380 K under 0.03 T after a zero-field-cooling (ZFC) process from 300 K to 200 K, as shown in Figure 2a. Therefore, by taking one derivative of the *M-T* curves, the Curie temperature of the $Fe_{88}Zr_{8-x}Sm_xB_4$ AA samples was determined to be 292 K for x = 0, 317 K for x = 2, and 348 K for x = 4. The Sm addition dramatically improved the T_c of the $Fe_{88}Zr_8B_4$ AAs.

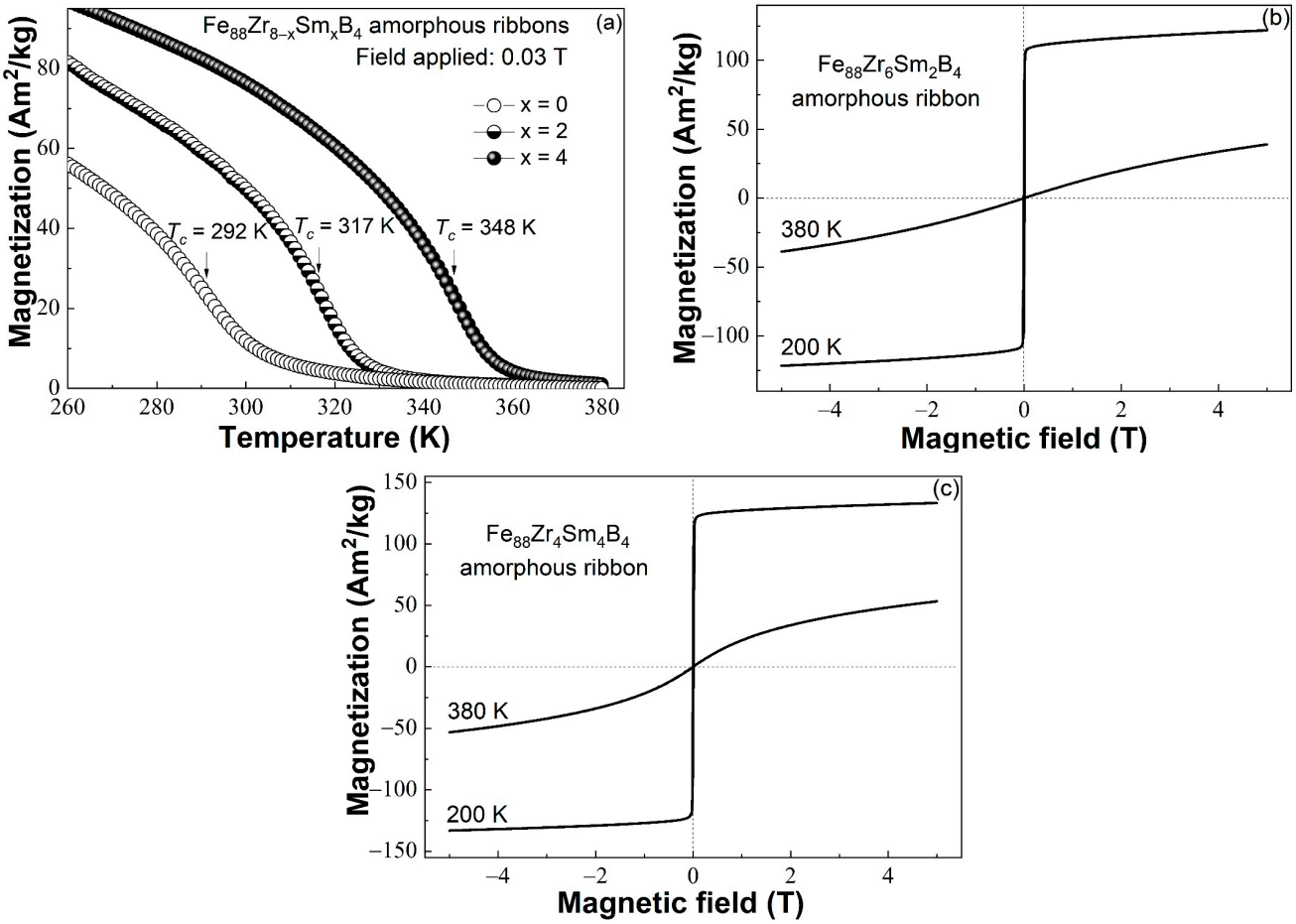

Figure 2. (**a**) The *M-T* curves of the $Fe_{88}Zr_{8-x}Sm_xB_4$ (x = 0, 2, 4) amorphous ribbons; the hysteresis loops of the (**b**) $Fe_{88}Zr_6Sm_2B_4$ and (**c**) $Fe_{88}Zr_4Sm_4B_4$ amorphous ribbons measured at 200 K and 380 K under 5 T.

The hysteresis loops of the $Fe_{88}Zr_{8-x}Sm_xB_4$ (x = 2, 4) AAs measured under 5 T at 200 K and 380 K are illustrated in Figures 2b and 2c, respectively. Both the samples were soft-magnetic at 200 K and paramagnetic at 380 K. The saturation magnetization (M_s) reached 127 Am^2/kg for the $Fe_{88}Zr_6Sm_2B_4$ amorphous sample and 139 Am^2/kg for the $Fe_{88}Zr_4Sm_4B_4$ sample. The saturation magnetization of the $Fe_{88}Zr_8B_4$ metallic

glass (104 Am^2/kg at 200 K [32]) was obviously improved by the Sm substitution, which indicated a better magnetocaloric performance of the Sm-doped samples because both the M_s and the $-\Delta S_m^{peak}$ of the amorphous samples depended mainly on their ordering of magnetic moments.

3.4. Magnetocaloric Performance of the $Fe_{88}Zr_{8-x}Sm_xB_4$ (x = 2, 4) AAs

Magnetic entropy changes in AAs are usually derived from their isothermal magnetization (*M-H*) curves measured at different temperatures. Figure 3 shows the *M-H* curves of the (a) $Fe_{88}Zr_6Sm_2B_4$ and (b) $Fe_{88}Zr_4Sm_4B_4$ amorphous samples. Thus, we calculated the $-\Delta S_m$ at different temperatures ($-\Delta S_m$-*T* curve) of the $Fe_{88}Zr_{8-x}Sm_xB_4$ metallic glasses according to the Maxwell equation [42]. The $-\Delta S_m$-*T* curves of the $Fe_{88}Zr_{8-x}Sm_xB_4$ ribbons under different applied fields are depicted in Figure 4a,b. The $-\Delta S_m^{peak}$ of the two samples under 1 T, 1.5 T, 2 T, 3 T, 4 T, and 5 T are summarized in Table 2. As expected above, the $-\Delta S_m^{peak}$ under 5 T reached 3.53 J/(K × kg) near 317 K for the $Fe_{88}Zr_6Sm_2B_4$ ribbon and 3.79 J/(K × kg) near 348 K for the $Fe_{88}Zr_4Sm_4B_4$ ribbon, both of which were much higher than those of the $Fe_{88}Zr_8B_4$ AA and other Fe-Zr-B-based amorphous ribbons [28,31–33]. As a result, the minor Sm substitution for Zr improved the magnetocaloric performance of the $Fe_{88}Zr_8B_4$ metallic glass.

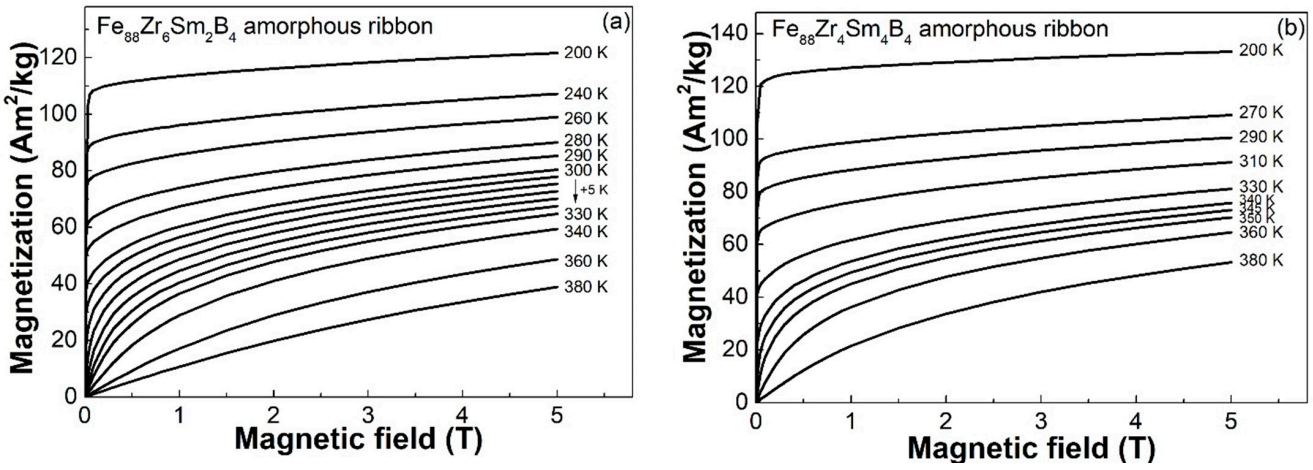

Figure 3. The isothermal magnetization curves of the (**a**) $Fe_{88}Zr_6Sm_2B_4$ and (**b**) $Fe_{88}Zr_4Sm_4B_4$ amorphous ribbons at various temperatures ranging from 200 K to 380 K under 5 T.

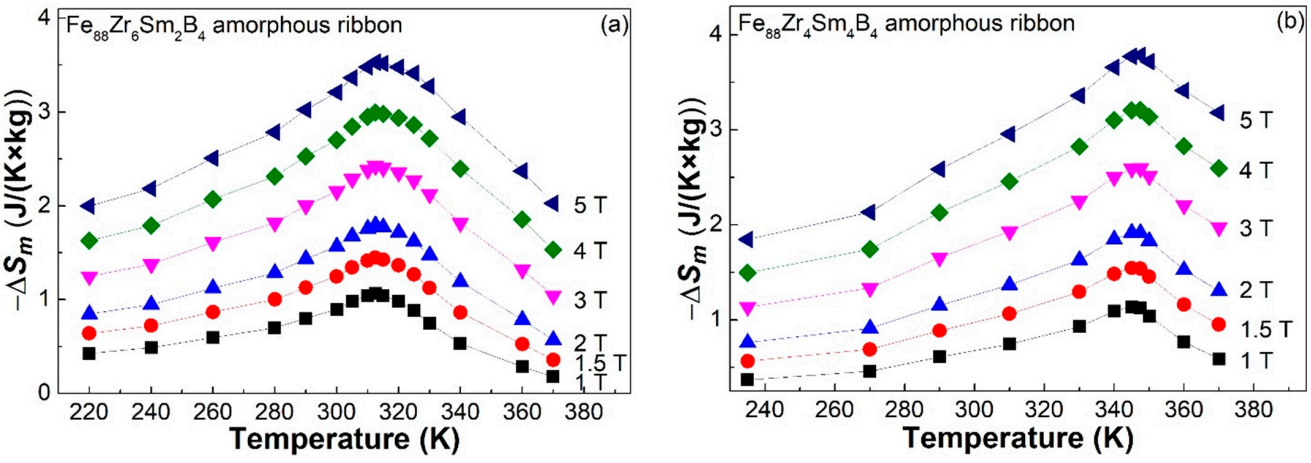

Figure 4. *Cont.*

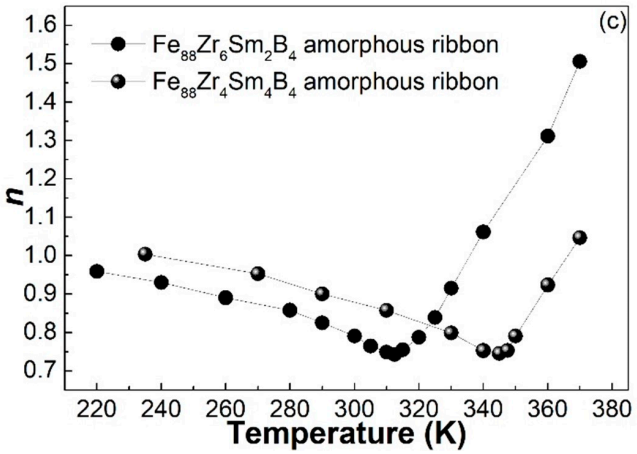

Figure 4. The $-\Delta S_m$-T curves of the (**a**) $Fe_{88}Zr_6Sm_2B_4$ and (**b**) $Fe_{88}Zr_4Sm_4B_4$ amorphous ribbons under various magnetic fields; (**c**) the temperature dependence of the exponent n for the $Fe_{88}Zr_{8-x}Sm_xB_4$ (x = 2, 4) amorphous ribbons.

Table 2. T_c and $-\Delta S_m{}^{peak}$ of the $Fe_{88}Zr_{8-x}RE_xB_4$ (RE = Sm, Nd, Pr; x = 0, 2, 4) amorphous alloys.

Composition	$-\Delta S_m{}^{peak}$ (J/(kg × K))						T_c (K)	Refs.
	1 T	1.5 T	2 T	3 T	4 T	5 T		
$Fe_{88}Zr_6Sm_2B_4$ [a]	1.07	1.45	1.79	2.42	3.00	3.53	317	Present work
$Fe_{88}Zr_4Sm_4B_4$ [a]	1.14	1.54	1.92	2.59	3.21	3.79	348	
$Fe_{88}Zr_8B_4$	0.87	1.20	1.50	2.06	2.57	3.04	292	[32]
$Fe_{88}Zr_6Nd_2B_4$	1.09	1.49	1.84	2.50	3.09	3.65	314	[35]
$Fe_{88}Zr_4Nd_4B_4$	1.20	1.65	2.05	2.79	3.47	4.10	335	
$Fe_{88}Zr_6Pr_2B_4$	1.07	1.47	1.82	2.46	3.05	3.60	306	[34]
$Fe_{88}Zr_4Pr_4B_4$	1.20	1.63	2.02	2.74	3.39	4.00	323	

[a] These results were obtained for the first time.

The magnetocaloric behaviors described by the n-T curves of the $Fe_{88}Zr_{8-x}Sm_xB_4$ amorphous samples are depicted in Figure 4c, where n is the slope of the linear fit for the $\ln(-\Delta S_m)$ vs. $\ln(H)$ plots. The shape of the n-T curves of the $Fe_{88}Zr_{8-x}Sm_xB_4$ metallic glass ribbons was similar to those of other amorphous alloys [32,43]. The minimum n value was ~0.74 at 312.5 K for the $Fe_{88}Zr_6Sm_2B_4$ ribbon and ~0.745 at 345 K for the $Fe_{88}Zr_4Sm_4B_4$ sample, both of which were close to the predicted value of fully amorphous alloys [43].

4. Discussion

4.1. Low-Temperature Magnetic Properties and Their Influence on the Magnetocaloric Properties of Sm-Doped $Fe_{88}Zr_8B_4$ AA Amorphous Ribbons

It is argued that the introduction of RE atoms to iron-based amorphous alloys may give rise to an interaction between Fe and the RE atoms, and lead to the formation of randomly oriented anisotropic clusters. The coupling between these anisotropic clusters may result in spin-glass freezing behaviors and large hysteresis at low temperatures [44–46], which may be harmful to the magnetocaloric performance of RE-doped Fe-based AAs. Therefore, it is essential to study the low-temperature magnetic properties of Fe-based AAs containing RE elements.

Fortunately, the spin-glass freezing behaviors and hysteresis are usually negligible when the RE concentration is very low because the anisotropic clusters are hard to couple with each other due to the low density of these clusters [34,35]. Therefore, we selected the $Fe_{88}Zr_4Sm_4B_4$ AA that contained the highest Sm content in the present work to study its low-temperature magnetic properties and their possible effect on the magnetocaloric properties in more detail.

Figure 5 shows the ZFC and field-cooling (FC, field applied: 0.03 T) *M-T* curves of the $Fe_{88}Zr_4Sm_4B_4$ AA sample. The ZFC *M-T* curve of the $Fe_{88}Zr_4Sm_4B_4$ AA ribbon almost overlapped the FC *M-T* curve, which implies that there was almost no spin-glass-like behavior in the $Fe_{88}Zr_4Sm_4B_4$ metallic glass. The hysteresis loop of the ribbon measured at 10 K is shown in the inset of Figure 5. Although the coercivity of the amorphous ribbon slightly increased compared to that of the $Fe_{88}Zr_8B_4$ alloy (~4.89 kA/m [32]), its value was only 8.61 kA/m at 10 K; in other words, it was negligible even at 10 K. The invisible spin-glass-like behavior and negligible coercivity at low temperatures indicate that the low-concentration Sm substitution for Zr did not induce an obvious interaction between random anisotropic clusters, and thus, barely affected the magnetocaloric performance of the AA.

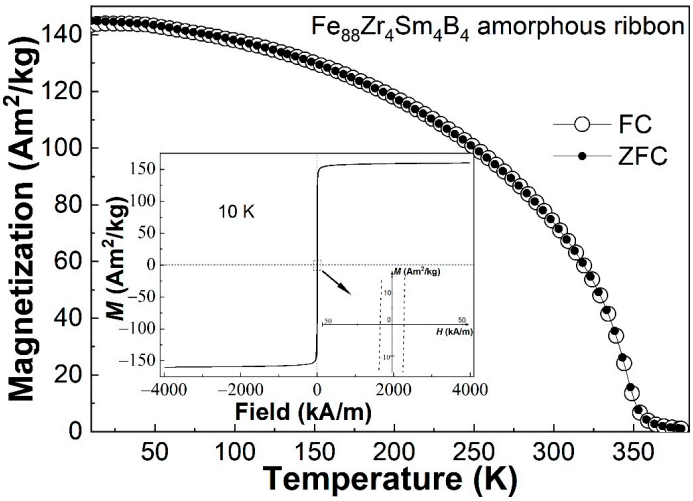

Figure 5. The ZFC and FC *M-T* curves of the $Fe_{88}Zr_4Sm_4B_4$ amorphous ribbon; the inset is the hysteresis loop of the $Fe_{88}Zr_4Sm_4B_4$ amorphous ribbon at 10 K.

4.2. The Compositional Dependence of T_c in RE-Doped $Fe_{88}Zr_8B_4$ AAs

As is known, the tailorable Curie temperature is one of the major characteristics of AAs that are superior to intermetallic alloys. Therefore, it is vitally important to understand the mechanism for the compositional dependence of T_c in these AAs. In the present work, the relationship between T_c and the Sm concentration in the $Fe_{88}Zr_{8-x}Sm_xB_4$ AAs was observed and compared to the dependence of T_c on the Nd and Pr content in the $Fe_{88}Zr_{8-x}RE_xB_4$ (RE = Nd, Pr) amorphous alloys. Figure 6a shows the T_c of the $Fe_{88}Zr_{8-x}RE_xB_4$ (RE = Sm, Nd, Pr; x = 0, 2, 4) amorphous ribbons. The T_c of the samples increased monotonously with the RE addition. The T_c of the Sm-doped AAs increased faster than that of the Nd-doped AAs, and much faster than that of the Pr-doped AAs. Previous works that focused on the compositional dependence of T_c in RE-TM-based AAs revealed that the T_c of these AAs is influenced by the direct TM-TM interaction as well as the indirect RE-RE and RE-TM interactions [47]. Both the direct TM-TM interaction and indirect RE-RE interaction have a similar impact on T_c in the RE-TM-based AAs; that is, T_c changes linearly with the TM concentration or RE concentration. The relationship between the indirect RE-TM interaction and T_c is more complicated and may exhibit an anti-parabolic shape. Fortunately, the negligible random magnetic anisotropy coupling mentioned above and the linear relationship between the T_c and the RE content indicate that the Fe-RE interaction in $Fe_{88}Zr_{8-x}RE_xB_4$ AAs may be very weak or ignorable due to the low concentration of RE. On the other hand, as the Fe concentration in $Fe_{88}Zr_{8-x}RE_xB_4$ is fixed, the effect of the direct Fe-Fe interaction on the Curie temperature did not need to be considered in the present work. Therefore, the T_c of the $Fe_{88}Zr_{8-x}RE_xB_4$ AAs depended mainly on the type of RE and its concentration. According to the Rudermann–Kittel–Kasuya–Yosida (RKKY)

indirect interaction model, T_c obeys a linear relationship with the de Gennes factor (G) of the RE in the AAs that contain only one rare earth element, as follows [48]:

$$T_c = \frac{2}{3k_B} I(0) G$$

where k_B is the Boltzman constant and $I(0)$ is the indirect exchange integral. From Figure 6a, one can find that T_c increases linearly with the RE concentration when the kind of RE is fixed, which is related to the linear increase in the indirect exchange integral with the addition of RE. On the other hand, as the G value is 4.44 for Sm, 3.20 for Nd, and 0.80 for Pr, the T_c of the $Fe_{88}Zr_{8-x}Sm_xB_4$ AAs is expected to be higher than the T_c of the $Fe_{88}Zr_{8-x}Nd_xB_4$ AAs and much higher than the T_c of the $Fe_{88}Zr_{8-x}Pr_xB_4$ AAs according to the equation when the RE concentration is fixed. Figure 6b shows the approximately linear dependence of T_c on the G values of Sm, Nd, and Pr when x = 2 and x = 4 of the $Fe_{88}Zr_{8-x}RE_xB_4$, both of which demonstrated that the T_c of the $Fe_{88}Zr_{8-x}RE_xB_4$ AAs is determined by the concentration and G value of the RE. The relationship between T_c and the de Gennes factor also implies the effectiveness of the de Gennes factor in determining or adjusting the T_c of RE-containing AAs.

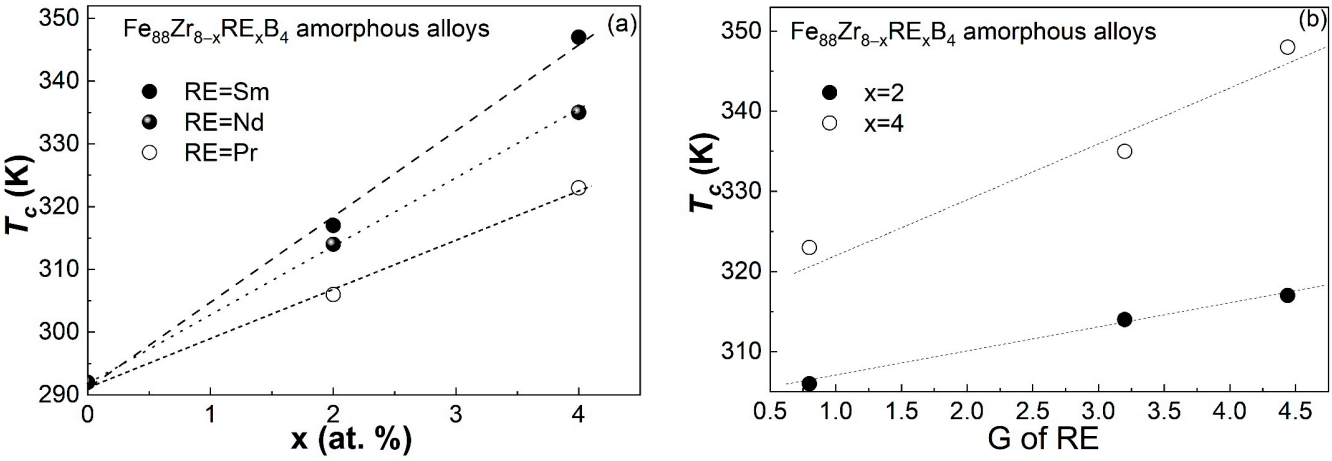

Figure 6. (**a**) The compositional dependence of T_c for the $Fe_{88}Zr_{8-x}RE_xB_4$ (RE = Sm, Nd, Pr; x = 0, 2, 4) amorphous alloys; (**b**) the relationship between the G values of different RE types and their T_c (solid circles represent x = 2 and hollow circles represent x = 4).

4.3. Magnetocaloric Performance of RE-Doped $Fe_{88}Zr_8B_4$ AAs

Figure 7a shows the $-\Delta S_m$-T curves under 5 T of the $Fe_{88}Zr_{8-x}Sm_xB_4$ AA ribbons, and the $Fe_{88}Zr_{8-x}Nd_xB_4$ as well as the $Fe_{88}Zr_{8-x}Pr_xB_4$ AAs for comparison purposes. Apparently, the $-\Delta S_m{}^{peak}$ of $Fe_{88}Zr_8B_4$ metallic glass was not only improved by a minor Sm substitution, but was also improved by Pr and Nd substitutions for Zr. Table 2 lists the $-\Delta S_m{}^{peak}$ under various magnetic fields of the $Fe_{88}Zr_{8-x}RE_xB_4$ (RE = Sm, Pr, Nd; x = 0, 2, 4) AAs. One can find that the improvement in the $-\Delta S_m{}^{peak}$ by the minor Sm addition was not as high as that resulting from the Pr and Nd additions at a fixed RE content; for example, the $-\Delta S_m{}^{peak}$ of the $Fe_{88}Zr_6Sm_2B_4$ amorphous ribbon at 5 T was ~3.53 J/(K × kg) at 317 K, which was lower than that of the $Fe_{88}Zr_6Pr_2B_4$ AA ribbon (~3.60 J/(K × kg) at 306 K [34]) and the $Fe_{88}Zr_6Nd_2B_4$ AA ribbon (~3.65 J/(K × kg) at 314 K [35]); the $-\Delta S_m{}^{peak}$ of the $Fe_{88}Zr_4Sm_4B_4$ amorphous ribbon at 5 T was ~3.79 J/(K × kg) at 348 K, which was lower than that of the $Fe_{88}Zr_4Pr_4B_4$ AA ribbon (~4.00 J/(K × kg) at 323 K [34]) and much lower than that of the $Fe_{88}Zr_6Nd_2B_4$ AA ribbon (~4.10 J/(K × kg) at 335 K [35]).

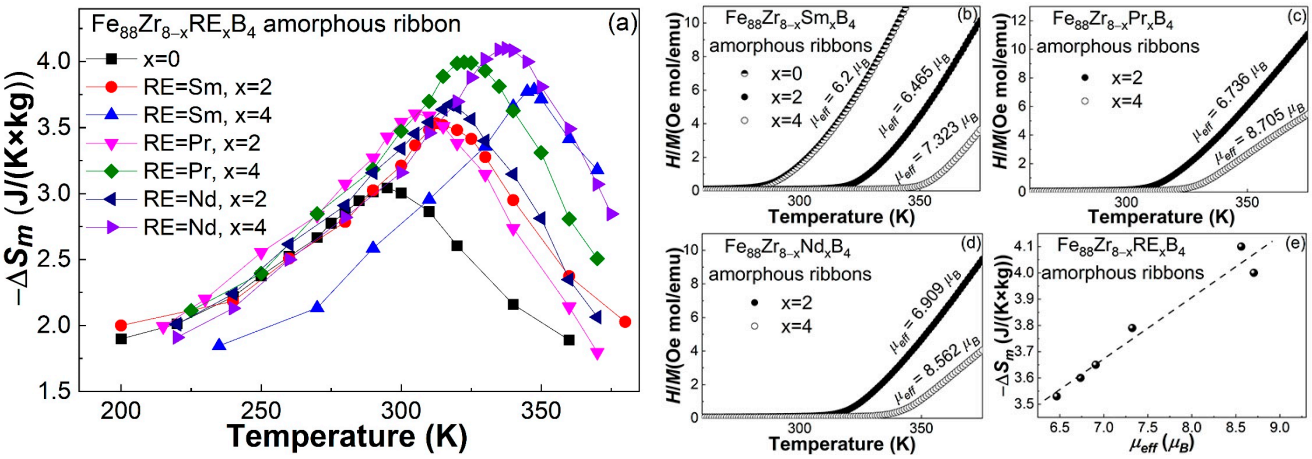

Figure 7. (**a**) The $-\Delta S_m$-T curves under 5 T of the $Fe_{88}Zr_{8-x}RE_xB_4$ (RE = Sm, Nd, Pr; x = 0, 2, 4) amorphous ribbons; the effective magnetic moment of the (**b**) $Fe_{88}Zr_{8-x}Sm_xB_4$ (x = 0, 2, 4), (**c**) $Fe_{88}Zr_{8-x}Pr_xB_4$ (x = 2, 4), and (**d**) $Fe_{88}Zr_{8-x}Nd_xB_4$ (x = 2, 4) amorphous alloys; and (**e**) the relationship between the $-\Delta S_m{}^{peak}$ and μ_{eff} of the $Fe_{88}Zr_{8-x}RE_xB_4$ (RE = Sm, Nd, Pr; x = 2, 4) amorphous alloys.

As the $-\Delta S_m$ of the AAs depends mainly on the ordering of magnetic moments upon magnetization, an enhancement in $-\Delta S_m{}^{peak}$ by a small amount of RE as a substitution for Zr may be closely related to the extra magnetic moment produced by the introduction of RE atoms. The addition of different kinds or contents of RE elements may result in different $-\Delta S_m$ improvements in the RE-doped amorphous alloys. As such, we attempted to calculate the effective magnetic moment (μ_{eff}) of the $Fe_{88}Zr_{8-x}RE_xB_4$ AAs from their M-T curves based on the Curie–Weiss law and Langevin function [49]. As shown in Figure 7b–d, the μ_{eff} of the $Fe_{88}Zr_{8-x}RE_xB_4$ amorphous ribbons was ~6.465 μ_B for RE = Sm and x = 2, ~7.323 μ_B for RE = Sm and x = 4, ~6.736 μ_B for RE = Pr and x = 2, ~8.705 μ_B for RE = Pr and x = 4, ~6.909 μ_B for RE = Nd and x = 2, and ~8.652 μ_B for RE = Nd and x = 4. Figure 7e shows the nearly linear relationship between the $-\Delta S_m{}^{peak}$ and the μ_{eff} of the $Fe_{88}Zr_{8-x}RE_xB_4$ AAs, which indicates that the $-\Delta S_m{}^{peak}$ of the minor RE-doped $Fe_{88}Zr_8B_4$ metallic glasses was closely related to their effective magnetic moment. Additionally, the μ_{eff} of the $Fe_{88}Zr_8B_4$ alloy was calculated to be ~6.2 μ_B, as shown in Figure 7b. It was found that the addition of an RE element obviously enhanced the μ_{eff} of the $Fe_{88}Zr_8B_4$ alloy. The increased $-\Delta S_m{}^{peak}$ and enhanced μ_{eff} suggest that an RE addition has a positive role in the improvement in the $-\Delta S_m{}^{peak}$ of Fe-based AAs.

5. Conclusions

$Fe_{88}Zr_{8-x}Sm_xB_4$ (x = 2, 4) amorphous samples with an average thickness of ~40 μm were successfully synthesized in this work. The GFA of the $Fe_{88}Zr_{8-x}Sm_xB_4$ (x = 2, 4) alloys was good enough for the 40-micrometer-thick amorphous ribbons. The effect of a Sm introduction on the magnetic and magnetocaloric performance of the $Fe_{88}Zr_8B_4$ AA and the mechanism involved were studied in more detail by comparing with those of other RE additions. The main conclusions are as follows:

(a) The minor Sm-doped $Fe_{88}Zr_8B_4$ AAs exhibited typical magnetocaloric behaviors of metallic glasses, and the invisible spin-glass-like behavior and negligible coercivity at low temperatures indicated that the minor Sm addition barely affected the magnetocaloric properties of the AAs.

(b) The T_c of the $Fe_{88}Zr_{8-x}Sm_xB_4$ AAs increased faster than those of the $Fe_{88}Zr_{8-x}Pr_xB_4$ and $Fe_{88}Zr_{8-x}Nd_xB_4$ AAs. The nearly linear relationship between the T_c and the de Gennes factor of Sm, Nd, and Pr when x = 2 and x = 4 demonstrated that the T_c of the $Fe_{88}Zr_{8-x}RE_xB_4$ AAs was determined by the concentration and G value of the RE.

(c) Although the $-\Delta S_m^{peak}$ of the $Fe_{88}Zr_8B_4$ AA was improved by the Sm substitution, the $-\Delta S_m^{peak}$ of the $Fe_{88}Zr_{8-x}Sm_xB_4$ was lower than that of the $Fe_{88}Zr_{8-x}Pr_xB_4$ and $Fe_{88}Zr_{8-x}Nd_xB_4$ amorphous ribbons when x = 2 and x = 4, respectively. The slightly lower $-\Delta S_m^{peak}$ of the Sm-doped AAs was closely related to their lower μ_{eff} according to the roughly linear relationship between the $-\Delta S_m^{peak}$ and the μ_{eff} of the $Fe_{88}Zr_{8-x}RE_xB_4$ AAs.

In brief, the mechanism of the change in the T_c and $-\Delta S_m^{peak}$ of the $Fe_{88}Zr_{8-x}RE_xB_4$ AAs was revealed, and an RE addition had a positive effect on the magnetocaloric performance of Fe-based AAs. These results are expected to be helpful for achieving excellent magnetocaloric AAs with a high $-\Delta S_m^{peak}$ at a tailorable T_c within the operating temperature interval of a domestic magnetic refrigerator.

Author Contributions: Conceptualization, L.X., P.Y. and J.-L.Y.; methodology, D.D.; validation, Q.W. and B.-Z.T.; investigation, Z.-R.Z., X.-J.L. and H.-T.Z.; data curation, Q.W. and D.D.; writing—original draft preparation, Z.-R.Z., X.-J.L. and H.-T.Z.; writing—review and editing, L.X. and Q.W.; funding acquisition, L.X. and P.Y. All authors have read and agreed to the published version of the manuscript.

Funding: This research was funded by the National Natural Science Foundation of China, grant numbers 51871139, 52071196, and 52071043.

Institutional Review Board Statement: Not applicable.

Informed Consent Statement: Not applicable.

Data Availability Statement: Data are contained within the article.

Acknowledgments: This research was technically supported by the Center for Advanced Microanalysis of Shanghai University.

Conflicts of Interest: The authors declare that they have no conflict of interest for this work.

References

1. Glanz, J. Making a Bigger Chill with Magnets. *Science* **1998**, *279*, 2045. [CrossRef]
2. Tegus, O.; Bruck, E.; Buschow, K.H.; de Boer, F.R. Transition-metal-based magnetic refrigerants for room-temperature applications. *Nature* **2002**, *415*, 150–152. [CrossRef]
3. Yu, B.F.; Gao, Q.; Zhang, B.; Meng, X.Z.; Chen, Z. Review on research of room temperature magnetic refrigeration. *Int. J. Refrig.* **2003**, *26*, 622–636. [CrossRef]
4. Brück, E. Topical review—Developments in magnetocaloric refrigeration. *J. Phys. D Appl. Phys.* **2005**, *38*, R381–R391. [CrossRef]
5. Franco, V.; Blázquez, J.S.; Ipus, J.J.; Law, J.Y.; Moreno-Ramírez, L.M.; Conde, A. Magnetocaloric effect: From materials research to refrigeration devices. *Prog. Mater. Sci.* **2018**, *93*, 112–232. [CrossRef]
6. Oliveira, N.; Ranke, P. Theoretical aspects of the magnetocaloric effect. *Phys. Rep.* **2010**, *489*, 89–159. [CrossRef]
7. Gschneidner, K.A., Jr.; Pecharsky, V.K.; Tsokol, A.O. Recent developments in magnetocaloric materials. *Rep. Prog. Phys.* **2005**, *68*, 1479–1539. [CrossRef]
8. Warburg, E. Magnetische Untersuchungen. *Ann. Phys.* **1881**, *249*, 141–164. [CrossRef]
9. Pecharsky, V.K.; Gschneidner, K.A., Jr. Giant magnetocaloric effect in $Gd_5(Si_2Ge_2)$. *Phys. Rev. Lett.* **1997**, *78*, 4494–4497. [CrossRef]
10. Shen, B.G.; Sun, J.R.; Hu, F.X.; Zhang, H.W.; Cheng, Z.H. Recent Progress in Exploring Magnetocaloric Materials. *Adv. Mater.* **2009**, *21*, 4545–4564. [CrossRef]
11. Pecharsky, V.K.; Gschneidner, K.A., Jr. Tunable magnetic regenerator alloys with a giant magnetocaloric effect for magnetic refrigeration from ~20 to ~290 K. *Appl. Phys. Lett.* **1997**, *70*, 3299–3301. [CrossRef]
12. Pasquale, M.; Sasso, C.P.; Lewis, L.H.; Giudici, L.; Lograsso, T.; Schlagel, D. Magnetostructural transition and magnetocaloric effect in $Ni_{55}Mn_{20}Ga_{25}$ single crystals. *Phys. Rev. B* **2005**, *72*, 094435. [CrossRef]
13. Miao, X.F.; Wang, W.Y.; Liang, H.X.; Qian, F.J.; Cong, M.Q.; Zhang, Y.J.; Muhammad, A.; Tian, Z.J.; Xu, F. Printing $(Mn,Fe)_2(P,Si)$ magnetocaloric alloys for magnetic refrigeration applications. *J. Mater. Sci.* **2020**, *55*, 6660–6668. [CrossRef]
14. Bouzidi, W.; Mliki, N.; Bessais, L. Second-order magnetic transition and low field magnetocaloric effect in nanocrystalline Pr_5Co_{19} compound. *J. Electron. Mater.* **2018**, *47*, 2776–2781. [CrossRef]
15. Hernández-González, E.L.; Watts, B.E.; Palomares-Sánchez, S.A.; Elizalde Galindo, J.T.; Mirabal-García, M. Second-order magnetic transition in $La_{0.67}Ca_{0.33-x}Sr_xMnO_3$ (x = 0.05, 0.06, 0.07, 0.08). *J. Supercond. Nov. Magn.* **2016**, *29*, 2421–2427. [CrossRef]
16. Álvarez, P.; Sánchez Llamazares, J.L.; Gorria, P.; Blanco, J.A. Enhanced refrigerant capacity and magnetic entropy flattening using a two-amorphous FeZrB(Cu) composite. *Appl. Phys. Lett.* **2011**, *99*, 232501. [CrossRef]
17. Luo, Q.; Wang, W.H. Magnetocaloric effect in rare earth-based bulk metallic glasses. *J. Alloys Compd.* **2010**, *495*, 209–216. [CrossRef]

18. Hashimoto, T.; Kuzuhara, T.; Sahashi, M.; Inomata, K.; Tomokiyo, A.; Yayama, H. New application of complex magnetic materials to the magnetic refrigerant in an Ericsson magnetic refrigerator. *J. Appl. Phys.* **1987**, *62*, 3873. [CrossRef]
19. Bingham, N.S.; Wang, H.; Qin, F.; Peng, H.X.; Sun, J.F.; Franco, V.; Srikanth, H.; Phan, M.H. Excellent magnetocaloric properties of melt-extracted Gd-based amorphous microwires. *Appl. Phys. Lett.* **2012**, *101*, 102407. [CrossRef]
20. Inoue, A. Bulk amorphous and nanocrystalline alloys with high functional properties. *Mater. Sci. Eng. A* **2001**, *304–306*, 1–10. [CrossRef]
21. Greer, A.L.; Rutherford, K.L.; Hutchings, I.M. Wear resistance of amorphous alloys and related materials. *Int. Mater. Rev.* **2002**, *47*, 87–111. [CrossRef]
22. Liu, X.Y.; Barclay, J.A.; Gopal, R.B.; Földeàki, M.; Chahine, R.; Bose, T.K.; Schurer, P.J.; LaCombe, J.L. Thermomagnetic properties of amorphous rare-earth alloys with Fe, Ni, or Co. *J. Appl. Phys.* **1996**, *79*, 1630–1641. [CrossRef]
23. Xue, L.; Shao, L.L.; Luo, Q.; Shen, B.L. $Gd_{25}RE_{25}Co_{25}Al_{25}$ (RE = Tb, Dy and Ho) high-entropy glassy alloys with distinct spin-glass behavior and good magnetocaloric effect. *J. Alloys Compd.* **2019**, *790*, 633–639. [CrossRef]
24. Luo, Q.; Zhao, D.Q.; Pan, M.X.; Wang, W.H. Magnetocaloric effect in Gd-based bulk metallic glasses. *Appl. Phys. Lett.* **2006**, *89*, 81914. [CrossRef]
25. Yuan, F.; Li, Q.; Shen, B.L. The effect of Fe/Al ratio on the thermal stability and magnetocaloric effect of $Gd_{55}Fe_xAl_{45-x}$ (x=15–35) glassy ribbons. *J. Appl. Phys.* **2012**, *111*, 07A937. [CrossRef]
26. Zheng, Z.G.; Zhong, X.C.; Su, K.P.; Yu, H.Y.; Liu, Z.W.; Zeng, D.C. Magnetic properties and large magnetocaloric effects in amorphous Gd-Al-Fe alloys for magnetic refrigeration. *Sci. China Phys. Mech. Astron.* **2011**, *54*, 1267–1270. [CrossRef]
27. Liu, G.L.; Zhao, D.Q.; Bai, H.Y.; Wang, W.H.; Pan, M.X. Room temperature table-like magnetocaloric effect in amorphous $Gd_{50}Co_{45}Fe_5$ ribbon. *J. Phys. D Appl. Phys.* **2016**, *49*, 055004. [CrossRef]
28. Yu, P.; Zhang, J.Z.; Xia, L. Effect of boron on the magneto-caloric effect in $Fe_{91-x}Zr_9B_x$ (x = 3, 4, 5) amorphous alloys. *J. Mater. Sci.* **2017**, *52*, 13948–13955. [CrossRef]
29. Wang, Y.Y.; Bi, X.F. The role of Zr and B in room temperature magnetic entropy change of FeZrB amorphous alloys. *Appl. Phys. Lett.* **2009**, *95*, 262501. [CrossRef]
30. Álvarez, P.; Gorria, P.; Sánchez, M.; Barquín, L.F.; Blanco, J.A. The role of boron on the magneto-caloric effect of FeZrB metallic glasses. *Intermetallics* **2010**, *18*, 2464–2467. [CrossRef]
31. Wu, Y.B.; Wang, Q.; Tang, B.Z.; Pan, L.L.; Ding, D.; Xia, L. Outstanding glass formability and magneto-caloric effect of a $Fe_{85}Co_3Zr_5B_4Nb_3$ metallic glass. *J. Non-Cryst. Solids* **2021**, *566*, 120885. [CrossRef]
32. Zheng, X.N.; Wang, Q.; Yue, C.Y.; Li, A.L.; Ding, D.; Xia, L. Achieving higher magnetic entropy change peak at lower temperature by minor Ti substitution for Zr in the $Fe_{88}Zr_8B_4$ metallic glass. *Mod. Phys. Lett. B* **2023**, *37*, 2350032. [CrossRef]
33. Li, A.L.; Wang, Q.; Tang, B.Z.; Yu, P.; Ding, D.; Xia, L. Magnetocaloric effect of the $Fe_{87}M_8B_5$ (M = Zr, Ce) amorphous alloys. *Mater. Sci. Eng. B Adv.* **2022**, *286*, 116033. [CrossRef]
34. Wang, Q.; Ding, D.; Tang, B.Z.; Yu, P.; Chan, K.C.; Xia, L. Excellent magnetocaloric performance of a $Fe_{88}Zr_4Pr_4B_4$ amorphous alloy and its amorphous hybrids. *Intermetallics* **2023**, *161*, 107982. [CrossRef]
35. Wang, P.J.; Wang, Q.; Zheng, S.H.; Zhu, L.Z.; Ding, D.; Tang, B.Z.; Yu, P.; Yao, J.L.; Xia, L. Improvement of Curie temperature and magnetic entropy change of a $Fe_{88}Zr_8B_4$ metallic glass by minor Nd substitution. *J. Non-Cryst. Solids* **2023**, *611*, 122347. [CrossRef]
36. Inoue, A. Stabilization of metallic supercooled liquid and bulk amorphous alloys. *Acta Mater.* **2000**, *45*, 279–306. [CrossRef]
37. Zhang, T.; Inoue, A.; Masumoto, T. Amorphous Zr–Al–TM (TM=Co, Ni, Cu) Alloys with Significant Supercooled Liquid Region of Over 100 K. *Mater. Trans. JIM* **1991**, *32*, 1005–1010. [CrossRef]
38. Turnbull, D. Under what conditions can a glass be formed? *Contemp. Phys.* **1969**, *10*, 473–488. [CrossRef]
39. Lu, Z.P.; Liu, C.T. Glass formation criterion for various glass-forming systems. *Phys. Rev. Lett.* **2003**, *91*, 115505. [CrossRef]
40. Minouei, H.; Rizi, M.S.; Akbari, G.H.; Hong, S.I. Effect of residual nanocrystals on thermal stability and mechanical properties of metalloid-containing amorphous alloys. *Mater. Charact.* **2021**, *173*, 110914. [CrossRef]
41. Wang, C.H.; Wang, Q.; Tang, B.Z.; Zhou, X.; Ding, D.; Xia, L. Achieve good magneto-caloric response near the ambient temperature in a $Fe_{86}La_7B_5Ce_2$ amorphous ribbon. *J. Magn. Magn. Mater.* **2022**, *547*, 168954. [CrossRef]
42. Hashimoto, T.; Numasawa, T.; Shino, M.; Okada, T. Magnetic refrigeration in the temperature range from 10 K to room temperature: The ferromagnetic refrigerants. *Cryogenics* **1981**, *21*, 647–653. [CrossRef]
43. Franco, V.; Blázquez, J.S.; Conde, A. Field dependence of the magnetocaloric effect in materials with a second order phase transition: A master curve for the magnetic entropy change. *Appl. Phys. Lett.* **2006**, *88*, 222512. [CrossRef]
44. Du, J.; Zheng, Q.; Brück, E.; Buschow, K.H.J.; Cui, W.B.; Feng, W.J.; Zhang, Z.D. Spin-glass behavior and magnetocaloric effect in Tb-based bulk metallic glass. *J. Magn. Magn. Mater.* **2009**, *321*, 413–417. [CrossRef]
45. Luo, Q.; Schwarz, B.; Mattern, N.; Eckert, J. Irreversible and reversible magnetic entropy change in a Dy-based bulk metallic glass. *Intermetallics* **2012**, *30*, 76–79. [CrossRef]
46. Luo, Q.; Schwarz, B.; Mattern, N.; Eckert, J. Giant irreversible positive to large reversible negative magnetic entropy change evolution in Tb-based bulk metallic glass. *Phys. Rev. B* **2010**, *82*, 024204. [CrossRef]
47. Zhang, H.Y.; Tan, J.; Zhang, X.; Yan, J.Z.; Shi, H.; Zhu, Y.; Cheng, W.Z.; Li, H.L.; Li, W.H.; Xia, A.L. Correlation between Magnetocaloric Properties and Magnetic Exchange Interaction in $Gd_{54}Fe_{36}B_{10-x}Si_x$ Amorphous Alloys. *Materials* **2023**, *16*, 3629. [CrossRef]

48. Zhang, H.Y.; Li, R.; Zhang, L.L.; Zhang, T. Tunable magnetic and magnetocaloric properties in heavy rare-earth based metallic glasses through the substitution of similar elements. *J. Appl. Phys.* **2014**, *115*, 133903. [CrossRef]
49. Matsumoto, N.; Shimosaka, T. Validation of a quantitative analytical method based on the effective magnetic moment and the Curie–Weiss law. *Accred. Qual. Assur.* **2015**, *20*, 115–124. [CrossRef]